AGU ADVANCING EARTH AND SPACE SCIENCE

Geophysical Research Letters

Key Points:
- Observations at the western Getz Ice Shelf show eight intermittent events of Winter Water deepening below 350 m depth during winter 2016
- The events are associated with strong easterly winds and caused by non-local Ekman downwelling
- The ocean heat transport into the Getz Ice Shelf cavity is reduced by 25% in the winter of 2016 due to the events

Intermittent Reduction in Ocean Heat Transport Into the Getz Ice Shelf Cavity During Strong Wind Events

Nadine Steiger[1,2] , **Elin Darelius**[1,2] , **Anna K. Wåhlin**[3] , and **Karen M. Assmann**[4]

[1]Geophysical Institute, University of Bergen, Bergen, Norway, [2]Bjerknes Center for Climate Research, Bergen, Norway, [3]Department of Marine Sciences, University of Gothenburg, Gothenburg, Sweden, [4]Institute of Marine Research, Tromsø, Norway

Abstract The flow of warm water toward the western Getz Ice Shelf along the Siple Trough, West Antarctica, is intermittently disrupted during short events of Winter Water deepening. Here we show, using mooring records, that these 5–10 days-long events reduced the heat transport toward the ice shelf cavity by 25% in the winter of 2016. The events coincide with strong easterly winds and polynya opening in the region, but the Winter Water deepening is controlled by non-local coastal Ekman downwelling rather than polynya-related surface fluxes. The thermocline depth anomalies are forced by Ekman downwelling at the northern coast of Siple Island and propagate to the ice front as a coastal trapped wave. During the events, the flow at depth does no longer continue along isobaths into the ice shelf cavity but aligns with the ice front.

Plain Language Summary Ocean-driven melting of the floating ice shelves that fringe the West Antarctica Ice Sheet has increased during the last decades. The transport of ocean heat toward the base of the ice shelves displays a large variability on daily to decadal timescales; still, the processes behind this variability are not well known. The western Getz Ice Shelf in West Antarctica experienced a persistent inflow of warm ocean water during 2016–2017, but the inflow was disrupted by intermittent events of reduced heat transport. The causes for these events are studied here, and it appears that atmospheric processes in the form of surface winds and locally reduced sea ice cover are important. Strong easterly winds push the sea ice off-coast and depress the cold surface waters toward the ocean floor. This deepening of the cold layer happens about 100 km away from the mooring site, but influences the heat transport under the ice shelf remotely through waves traveling along the coast. Simultaneously, the ocean currents are deflected at the ice front, which causes a substantial decrease of the heat transport toward the base of the ice shelves during these events.

1. Introduction

Increased oceanic heat transport toward the ice shelves has been the primary driver of ice-shelf thinning in the Amundsen Sea sector of West Antarctica during the last decades (Jenkins et al., 2018; Pritchard et al., 2012; Rignot et al., 2013, 2019). The oceanic heat transport is associated with the flow of warm Circumpolar Deep Water (CDW) onto the continental shelf, mainly controlled by wind forcing at the continental shelf break (Assmann et al., 2019; Dotto et al., 2019; Gille et al., 2016; Jenkins, 2016; Steig et al., 2012; Thoma et al., 2008; Wåhlin et al., 2013). The CDW accesses the continental shelf through submarine troughs that steer the warm water toward the ice shelves and into their underlying cavities (Arneborg et al., 2012; Thoma et al., 2008; Wåhlin et al., 2010; Walker et al., 2007). Once it reaches the ice shelf base, the warm water induces basal melting and ice shelf thinning, leading to acceleration of the upstream ice (Reese et al., 2018) and consequent sea level rise (DeConto & Pollard, 2016). The glacial meltwater may influence the ocean circulation (Nakayama et al., 2014), sea ice production (Jourdain et al., 2017), melt rates of nearby ice shelves (Jourdain et al., 2017) and dense water formation (Jacobs et al., 2002; Nakayama et al., 2014; Silvano et al., 2018). This motivates studies of the variability in ocean heat supply to the base of the ice shelves, which is especially complex in the Amundsen Sea, a region of high atmospheric variability (Raphael et al., 2016; Thoma et al., 2008).

The Getz Ice Shelf (GIS) is, with 33,200 km^2, the largest ice shelf in the Amundsen Sea, and it is the largest freshwater source in this region. It has an average melt rate of about 4 m yr^{-1} (Depoorter et al., 2013;
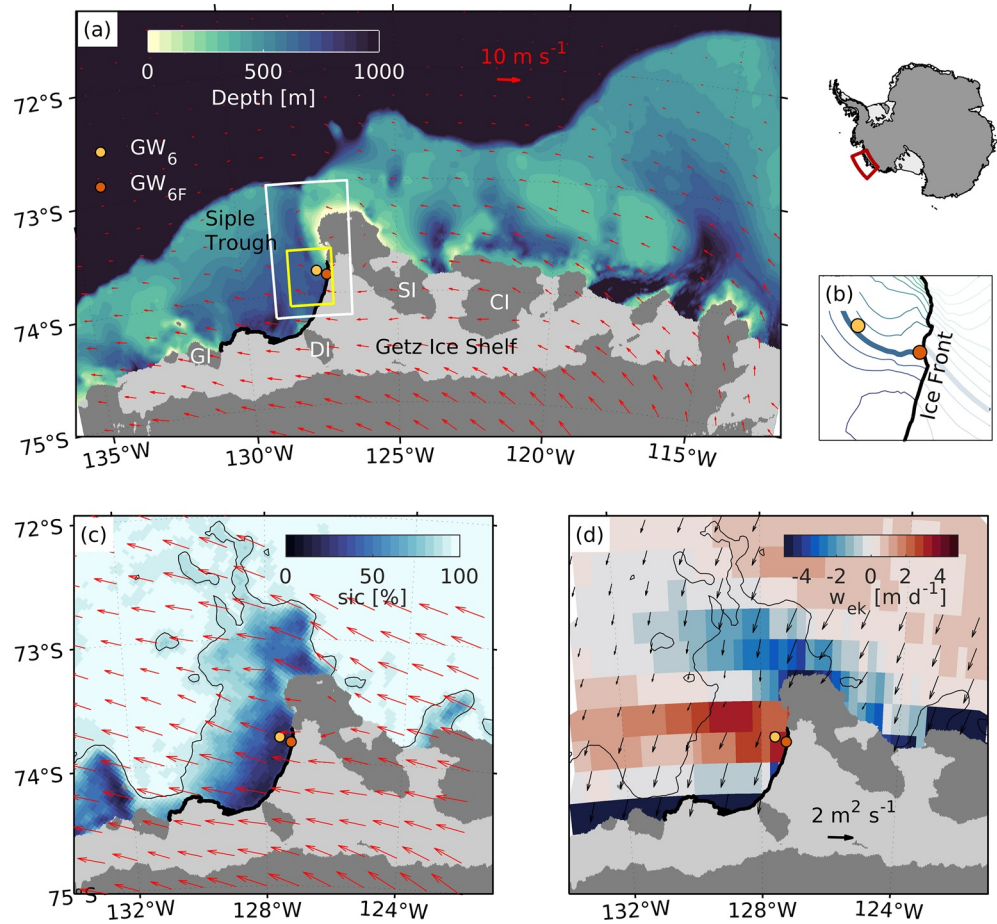
Figure 1. (a) Map of the Getz Ice Shelf area. The bathymetry (color) from the international bathymetric chart of the Southern Ocean (IBCSO) data set (Arndt et al., 2013) is overlaid by the mean (January 2016–January 2018) 10 m winds (red vectors) from ERA5 (Hersbach et al., 2018). The island names from west to east are: DI = Dean Island, SI = Siple Island, GI = Grant Island, CI = Carney Island. The white (yellow) box shows the area over which 10 m winds and sea ice concentration (surface heat flux) shown in Figure 2 are averaged. (b) Zoomed map of the mooring area showing the ice front position in January 2016 (bold black) and bathymetry contours every 50 m with the 600 m isobath in bold. (c) Ensemble average of the sea ice concentration from AMSR2 (Spreen et al., 2008) (color) and 10 m wind (red vectors, same velocity scale as in (a)). (d) Ensemble average of the vertical Ekman velocity (w_{ek}, color) overlaid by the Ekman transport (black vectors). The ensemble averages in (c) and (d) are taken 3 days ahead of the heat content minima marking the events, thus, when the winds are strongest. The black thin contour in (c) and (d) marks the 90% sea ice concentration. The location of GW_6 (GW_{6F}) are marked with a yellow (orange) circle in all panels. Ice shelf (light gray) and grounded ice/land (dark gray) masks in (a,c, and d) are from the RTOPO2 bathymetry data set (Schaffer et al., 2016), updated between SI and GI with the observed ice front position (bold black line).

Rignot et al., 2013) and accounts for about 50% of all ice loss from the Amundsen Sea ice shelves (Paolo et al., 2015). Still, the western GIS and the adjacent ocean are little studied compared to ice shelves further east in the Amundsen Sea, for example, the Thwaites and the Pine Island Ice Shelf, which have larger basal melt rates (Paolo et al., 2015; Pritchard et al., 2012) and are supposedly exposed to larger volumes of CDW (Jacobs et al., 2012, 2013). The GIS has several ice fronts, most of which are located above a trough in the ocean floor (Figure 1a). The hydrography in these troughs differs largely. While bottom temperatures are only about 0°C just east of Siple Island (Jacobs et al., 2013), they reach up to 1.5°C west of Siple Island, which is the highest temperature observed at any ice front in the Amundsen Sea (Assmann et al., 2019). The warm CDW is carried toward the ice front by a current that flows southward along the eastern flank of the Siple Trough (Assmann et al., 2019). The current has a barotropic (depth-independent, typically wind-driven) and a baroclinic (depth-varying, set up by density gradients) component (Wåhlin et al., 2020). At the ice front, the barotropic component is deflected, so that only the heat transport associated with the

smaller baroclinic component enters the ice shelf cavity (Wåhlin et al., 2020). In this study, we explore the variability of the heat transport into the GIS cavity west of Siple Island on a daily to weekly timescale and provide insights into the link between atmospheric forcing and the heat supply to the cavity.

The heat content variability on the Amundsen Sea continental shelf has so far mainly been explained by wind-driven changes in the transport of CDW across the shelf break onto the continental shelf (Dutrieux et al., 2014; Kim et al., 2017; Thoma et al., 2008; Wåhlin et al., 2013; Webber et al., 2019). Surface processes that influence the heat transport across the continental shelf to the ice shelves, however, have been investigated less due to the scarcity of year-round observations on the continental shelf, especially of the surface waters. Surface heat fluxes, sea ice growth and surface winds over the continental shelf may modify the water masses and the depth of the thermocline, which separates the warm and saline CDW from the overlaying cold and fresh Winter Water (WW). The thermocline depth relative to the ice shelf draft affects basal melt rates (De Rydt et al., 2014; Dutrieux et al., 2014; Padman et al., 2012). In front of the Pine Island Glacier, deepening of the thermocline on seasonal to interannual timescales has been linked to surface heat fluxes in coastal polynyas (St-Laurent et al., 2015; Webber et al., 2017) and reduced basal melt rates (St-Laurent et al., 2015). Also in other regions around Antarctica, a similar oceanic response to coastal polynyas has been found (Årthun et al., 2013; Gwyther et al., 2014; Haid & Timmermann, 2013; Holland et al., 2010; Khazendar et al., 2013). The west coast of Siple Island is a favorable location for a coastal polynya (Ohshima et al., 2016) given its orientation perpendicular to the prevailing easterly winds, suggesting that a modification of the heat content through surface processes may be relevant here, too.

Fluctuations in the thermocline depth can further be related to the variability in vertical Ekman velocities driven by local winds. This process has been proposed as the main driver of melt rate variability beneath Pine Island Ice Shelf on weekly to monthly timescales (Davis et al., 2018). At the coast, Ekman pumping occurs through convergence and divergence of wind-driven Ekman transport and modifies the strength of the Antarctic Coastal Current that flows westward along the Antarctic coast (Kim et al., 2016; Spence et al., 2014). Variability in the coastal Ekman pumping might additionally induce coastal trapped waves—a hybrid between internal Kelvin waves and topographic Rossby waves—that propagate with the coast to the left in the Southern Hemisphere. Variations in thermocline depth at the coast might consequently be a response to remote wind forcing (Gill & Clarke, 1974). The importance of coastal Ekman pumping relative to surface fluxes within the coastal polynya for the short term variability in the heat transport toward the GIS cavity has not been quantified.

Here, we describe events of intermittent deepening of the cold WW in front of the GIS west of Siple Island and investigate their drivers and implications. The mooring data cover a two-year period (from January 2016 to January 2018) and the moorings were deployed at a distance of 11 km and about 800 m from the ice front. We discuss possible atmospheric drivers of the WW deepening involving winds and sea ice formation. We also discuss the events in relation to the blocking of the barotropic component found at the GIS (Wåhlin et al., 2020) and investigate the consequent implications for the variability of the heat transport into the ice shelf cavity.

2. Data and Methods

We use observations from two moorings that were deployed from January 29, 2016 to January 18, 2018 close to the GIS front west of Siple Island (Assmann et al., 2019, Figure 1a). Both moorings were located on the 600 m isobath of the eastern flank of the Siple Trough at a distance of about 800 m (GW$_{6F}$, 73°50.0′S, 127°16.6′W) and 11 km (GW$_6$, 73°47.6′S, 127°36.0′W) from the 2016-ice front (Figure 1b). The moorings were equipped with temperature, conductivity, and pressure sensors from Seabird Electronics (SBE37, SBE39, and SBE56), and extended from the bottom to 357 and 288 m depth for GW$_6$ and GW$_{6F}$, respectively. GW$_6$ had a downward-looking Acoustic Doppler Current Profiler (ADCP; Teledyne RD Instruments, 150 kHz Sentinel) at the top of the mooring, and GW$_{6F}$ had an upward-looking ADCP at the bottom.

The hydrographic data in this study are presented as conservative temperature Θ (in °C) and absolute salinity S_A (in g kg^{-1}) using the TEOS-10 equation of state (McDougall & Barker, 2011). We define WW as water with a conservative temperature of $\Theta < -1.8$°C and CDW as water with $\Theta > 1$°C and $S_A > 34.85$ g kg^{-1}. The
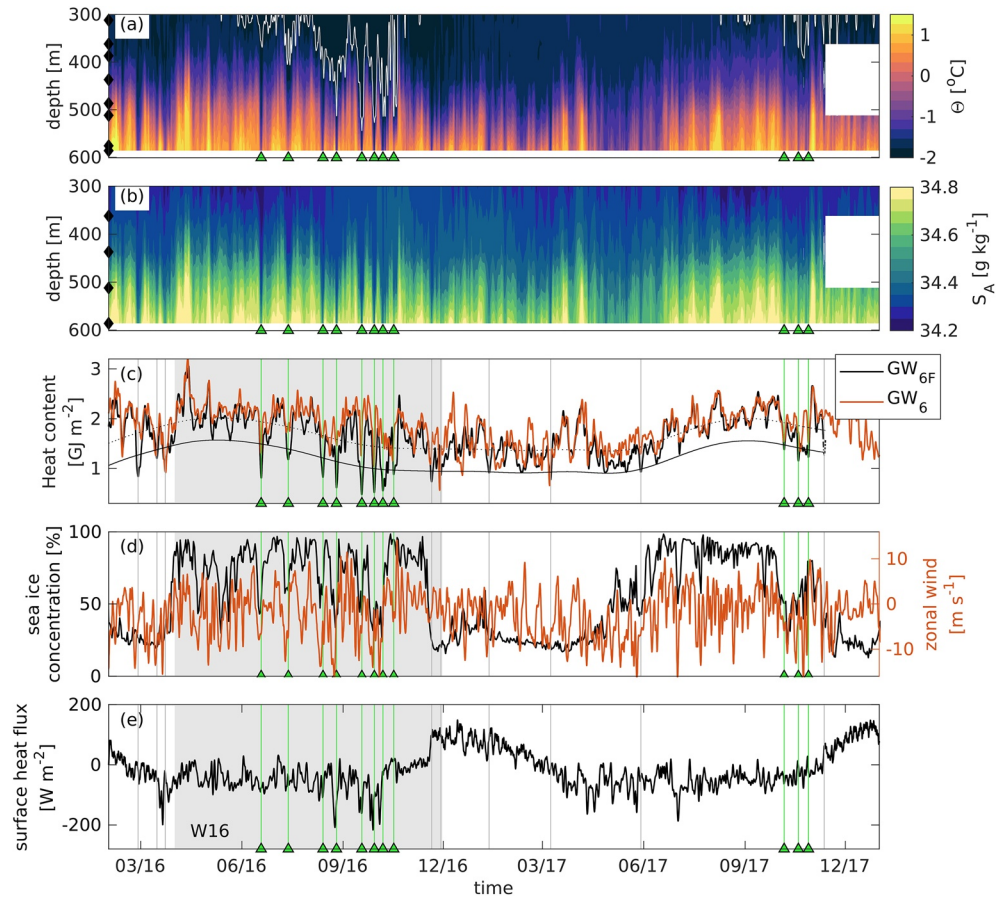
Figure 2. (a) Conservative temperature Θ from GW_{6F}. The white contour shows the depth of the Winter Water (WW) ($\Theta = -1.8°C$). The depths of the temperature sensors are marked with black diamonds on the y-axis. (b) Absolute salinity S_A from GW_{6F}. The depths of the conductivity sensors are marked with black diamonds on the y-axis. (c) Heat content at GW_{6F} and GW_6. The dotted black curve marks the 90 days lowpass filtered heat content at GW_{6F} and the solid black curve marks one standard deviation below, the threshold used to define the events. (d) Sea ice concentration from AMSR2 (Spreen et al., 2008) and 10 m zonal winds from ERA5 (Hersbach et al., 2018) averaged over the white box in Figure 1a. (e) Surface heat flux from ERA5 averaged over the yellow box in Figure 1a. In all time series, the local minima in heat content below the threshold are marked with vertical lines and the events of deepened WW are highlighted in green. The light gray shading in (c)–(e) shows the 2016 sea ice season (April–November; W16).

presented data are filtered with a second-order lowpass digital Butterworth filter with a normalized cutoff period of one day, unless otherwise stated.

The events of intermittent WW deepening are defined based on the heat content at GW_{6F} (Figure 2c). We identify local minima that are below one standard deviation (0.44 GJ/m^2) from the 90-days lowpass filtered heat content during periods when the WW is below 350 m depth (green markers in Figure 2). The five days before and after the heat content minimum are considered part of each event (Figures 3a–3c). We specifically focus on eight events within the 2016 sea ice season (April–November; W16).

The heat content, H, is calculated from the difference between the conservative temperature and the conservative temperature freezing point, Θ_f, according to:

$$H = \int_{z_2}^{z_1} \rho_w c_p (\Theta - \Theta_f) dz, \tag{1}$$

where ρ_w is the in-situ density, $c_p = 3{,}991.9$ J (kg K)$^{-1}$ is the specific heat capacity, and z_2 and z_1 are the depths of the lower and the upper temperature sensors. z is positive upwards, and $z = 0$ at the surface.
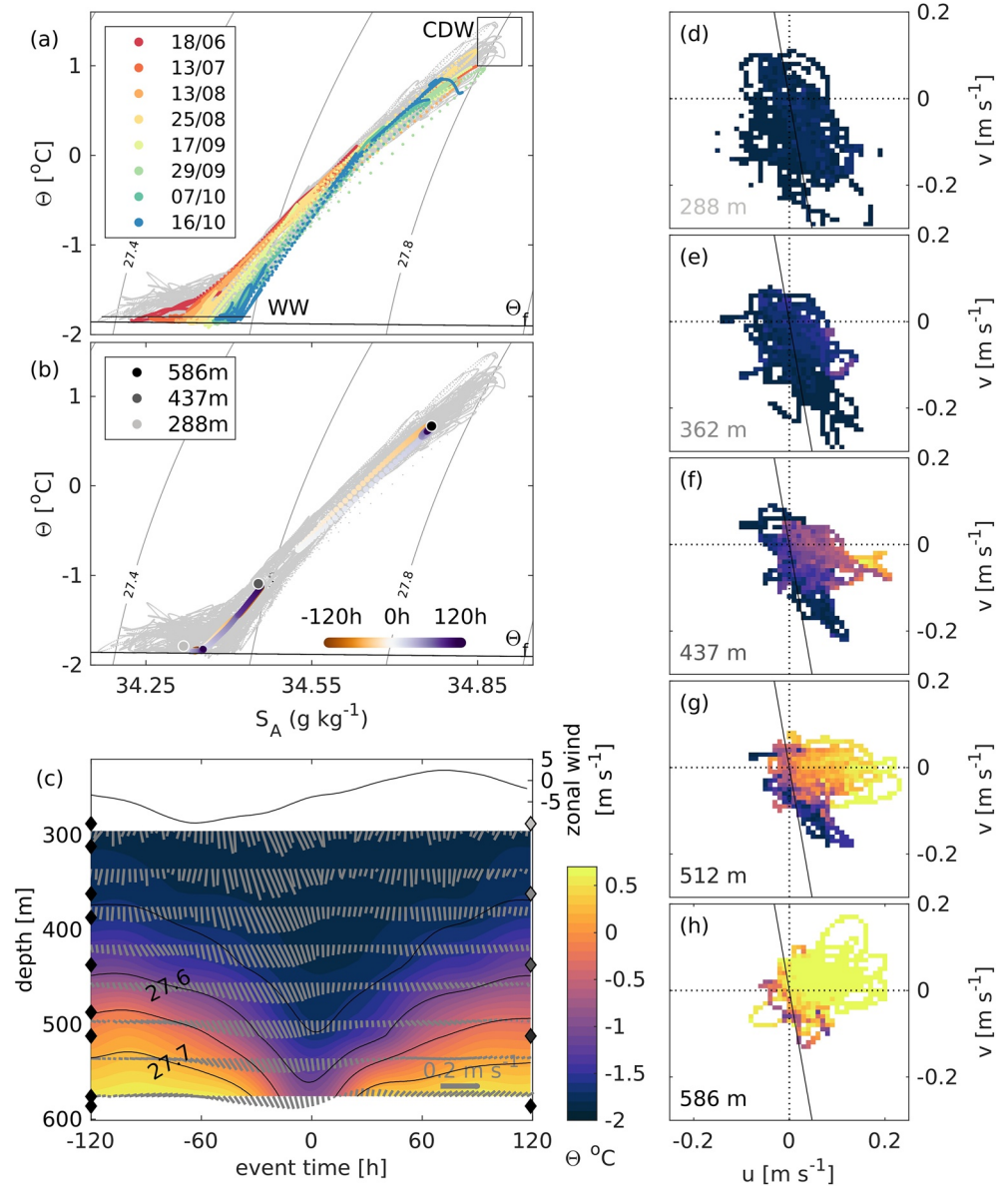
Figure 3. (a) and (b) Θ-S_A - plots from GW$_{6F}$. Gray dots show the data from the whole measurement period. The freezing line (Θ_f) and the properties of Winter Water (WW) and Circumpolar Deep Water (CDW) are marked. The color-coded dots show (a) each of the eight events in W16 (dates in the legend) (b) the event time for the ensemble average at 288, 437, and 586 m depth. The gray dots in (b) show the properties at the three depths averaged over W16. (c) Ensemble average of the 10 m zonal wind above, ensemble average of conservative temperature (color) and potential density anomaly (black contours) below, overlaid by the current velocity (up is north, right is east). Every second time step of the velocities is shown. Diamonds at the left y-axis mark the depth of temperature sensors and diamonds at the right y-axis mark the depths of the conductivity sensors, shown in (d)–(h). (d)–(h) 2D scatter plot of the current velocity components color-coded with conservative temperature averaged over W16 at different depths. The black line shows the bearing of the ice front in the vicinity of GW$_{6F}$ (Figure 1b).

The temperature at the upper sensor of GW$_{6F}$ (at 288 m depth) is on average only 0.08°C above the surface freezing point and remains below $\Theta = -1.6$°C during W16. The heat content above the upper sensor is consequently assumed to be small.

The heat transport per unit width, referred to as the heat transport density, Q, toward the ice shelf is found by including the velocity component perpendicular to the local ice front, u_r, in the integration of Equation 1, as:

$$Q = \int_{z_2}^{z_1} \rho_w c_p u_r (\Theta - \Theta_f) dz. \tag{2}$$

To analyze atmospheric drivers, we use 10 m winds and surface heat fluxes from ERA5 hourly reanalysis data available on a $0.25° \times 0.25°$ grid (Hersbach et al., 2018). Daily mean sea ice concentration data are obtained on a 3.125 km grid from AMSR-E/AMSR2 satellite remote sensing observations (Spreen et al., 2008). We mask the sea ice concentration based on ice/land masks from the RTOPO2 bathymetry data set (Schaffer et al., 2016), corrected between Siple Island and Grant Island with the ice front position in January 2016 (Figure 1a; Wåhlin et al., 2020). The ice front west of Siple Island is generally facing west-northwest, but the local ice front closest to GW_{6F} is facing west-southwest with a local bearing of 170° from true north (Figure 1b). The orientation did not change during 2016, but the front advanced about 250 m between January 2016 and January 2017.

The horizontal Ekman transport, m_{ek}, and the vertical Ekman velocities, w_{ek}, are calculated as

$$\boldsymbol{m_{ek}} = -\frac{1}{\rho_0 f} \cdot \boldsymbol{k} \times \boldsymbol{\tau} \tag{3}$$

$$w_{ek} = \frac{1}{\rho_0} \cdot \nabla \times \left(\frac{\boldsymbol{\tau}}{f}\right), \tag{4}$$

where f ($f < 0$) is the Coriolis parameter, k is the unit vector in z-direction, $\rho_0 = 1{,}027$ kg m^{-3} is the ocean water density. The ocean surface stress τ is here calculated as the wind stress:

$$\boldsymbol{\tau} = \rho_a C_{aw} \mid \boldsymbol{u_a} \mid \boldsymbol{u_a}, \tag{5}$$

where $\rho_a = 1.25$ kg m^{-3} is the air density, $C_{aw} = 1.25 \times 10^{-3}$ is the air-water drag coefficient, and u_a is the 10 m wind vector. In ice-covered regions, τ is a combination of surface air-ocean stress over open water and ice-ocean stress beneath sea ice (e.g., Dotto et al., 2018). However, the existing sea ice drift data (Polar Pathfinder Daily 25 km EASE-Grid Sea Ice Motion Vectors; Tschudi et al., 2019) do not cover the coastal region and are known to be of poor quality in the Southern Ocean (Tschudi et al., 2020). Since the sea ice concentration is low here during the events, we argue that air-ocean stresses provide a good first-order estimate for the coastal Ekman pumping. Results from calculations of the Ekman transport and pumping for a τ that includes ice-ocean stresses, based on existing sea ice drift data and estimated sea ice velocity from surface winds (Kimura, 2004), agree qualitatively (Supporting Information, Figure S1).

3. Results and Discussion

3.1. Cold Events

The temperature record from the near-front mooring GW_{6F} shows eight short-term events of deepened WW in W16 that disrupt the flow of relatively warm water toward the GIS cavity (Figure 2a; Assmann et al., 2019). The $-1.8°C$-isotherm, which marks the depth of the WW, deepens by 50–200 m during these events and reaches a maximum depth of 550 m. The events last about 4–10 days from the onset of the deepening to the relaxation and are most noticeable at depth. The bottom temperature at 586 m depth drops by 1–2°C during the events from a two-year mean temperature of $\Theta = 0.53 \pm 0.50°C$. A reduction in heat content during the events is also evident at GW_6, although with a smaller magnitude (Figure 2c). The heat content at GW_{6F} correlates strongly with the heat content at GW_6 ($r = 0.84$ on a 99% significance level), where GW_{6F} lags GW_6 with 6 h.

The temperature and salinity correlate strongly ($r = 0.99$ at a 99% significance level) at the two lowermost sensors (at 586 and 512 m depth), and the reduction in temperature at depth is accordingly accompanied by reduced salinity (Figure 2b). The sensors above 400 m depth show little variation in temperature and salinity during W16. The difference in density between the two uppermost sensors at 288 and 362 m depth is below 0.04 kg m^{-3} between August and November 2016; thus the surface mixed layer, defined as

$\frac{\Delta\rho}{\Delta p} < 0.0005$ kg m^{-3} dbar^{-1} based on the potential density ρ (Holte & Talley, 2009), reaches down to these sensors during that time period (Figures 2b and 3b–3c). The surface mixed layer extends all the way to the bottom during the events (Figures 2a and 2b).

The events coincide with sudden drops in the local sea ice concentration and strong easterly winds (Figure 2d). The prevalent east-southeasterly winds are directed off-shore at the mooring site, and episodes with strong winds of about 12 m s^{-1} over a few days open up a coastal polynya. The winds peak about 50–70 h ahead of the minimum in heat content during the events. The polynya occurs along the ice front between Siple and Dean Island, where the moorings are located, and extends along the west coast of Siple Island (Figures 1c and 1d). North of Siple Island, sea ice diverges west of an area of fast ice and stranded icebergs (Mazur et al., 2017).

3.2. Driving Mechanisms

Mechanisms linked to atmospheric forcing have been found to modify the ocean heat content in the vicinity of ice shelves. Surface heat and salt fluxes in coastal polynyas lead to convection and deepening of the overlaying cold WW (Årthun et al., 2013; Khazendar et al., 2013; St-Laurent et al., 2015; Webber et al., 2017), while vertical Ekman velocities deepen the thermocline mechanically (Davis et al., 2018; Kim et al., 2016, 2017).

Heat loss in coastal polynyas can explain ocean heat content variability on seasonal to interannual timescales (Webber et al., 2017). However, the cumulative surface heat flux at the mooring site during individual events is only about 0.02 GJ m^{-2} (Figure 2e), two orders of magnitude below the intermittent heat loss of about 1 GJ/m^{-2} recorded in the water column. The contribution of sea ice production and melt to the total surface heat flux is not included in the surface heat flux estimates, but this is not expected to explain the discrepancy of two orders of magnitude (Webber et al., 2017).

The representation of the hydrography in temperature-salinity space shows that the water column is filled with warm and saline CDW, fresh and cold WW, and a mixture between the two water masses (Figures 3a and 3b). The Θ-S_A-diagram for each of the events shows a gradual densification of the upper water column (above 362 m depth) during W16 (Figure 3a). During the individual events, the hydrography evolves "back and forth" along the mixing line, with equal properties before and after the events (Figure 3b). This demonstrates that there is no major water mass transformation during the individual events, but a vertical movement of isopycnals.

Analysis of the temperature variability along isopycnal surfaces following Dotto et al. (2019) confirms that changes in temperature along isopycnal surfaces (i.e., changes in water mass properties) are only prominent in the upper part of the water column at long timescales (seasonal to interannual). In contrast, and in agreement with the Θ-S_A-analysis, the vertical displacement of isopycnal surfaces (i.e., mechanical deepening) acts at short timescales (several days) and explains most of the short-term variability in temperature at depth. Mechanically driven downwelling might also explain the drops in heat content that occur during the summer months, for instance in March 2016 (Figure 2c). This event coincides with strong easterly winds, but there is evidently no polynya activity, as sea ice formation has not started yet (Figure 2d).

Mechanical deepening of the thermocline results from wind-driven vertical motion. If winds are directed along-shore with the coast to the left in the Southern Hemisphere, onshore Ekman transport converges at the coast and drives downwelling (Gill & Clarke, 1974; Sverdrup, 1953). At the mooring site, however, winds as well as sea ice drift are directed off-shore during the events—resulting in the polynya openings—and the deepening of the thermocline is consequently not caused by local Ekman downwelling (Figures 1c and 1d, Figure S1). Instead, conditions favor converging Ekman transport and coastal downwelling at the northern coast of Siple Island (Figure 1d and Figure S1). We suggest that anomalies in thermocline depth caused by downwelling along the northern coast of Siple Island propagate toward the mooring site as coastal trapped waves. The mechanism is illustrated in Figure 3c. The maximum Ekman downwelling north of Siple Island occurs about 100 km upstream of GW$_{6F}$ (Figure 1a) and leads the heat content minimum by 50–70 h, suggesting a propagation speed along the coast of about 0.4–0.6 m s^{-1}.

The inferred propagation speed agrees qualitatively with the theoretical propagation speed of, for example, an internal Kelvin wave or a topographic Rossby wave. Considering a two-layered flat-bottom ocean with layer thicknesses of $H_1 = 350$–400 m and $H_2 = 200$–350 m, the first baroclinic mode gives a speed of an internal Kelvin wave of about $c = \sqrt{g' \dfrac{H_1 \cdot H_2}{H_1 + H2}} \approx 0.4 - 0.6$ m s^{-1}, where the reduced gravity is $g' \approx 1$–2×10^{-3} m s^{-2}.

The speed agrees well with the estimate from the observations, but the requirement for a Kelvin wave of a vertical wall is only satisfied at the ice front. The along-slope maximum propagation speed of a topographic Rossby wave is $c = g' \dfrac{\alpha}{f} \approx 0.2 - 0.4$ m s^{-1}, considering a linear slope of the west coast of Siple Island of $\alpha = 0.025$. We do not expect the observations to match exactly these theoretical values, as stratification (Gill & Clarke, 1974) and varying bed topography (Robinson, 1964) influence the wave speed, but both values agree qualitatively with the wave speed estimated from the observations. The estimated wave speed gives a Rossby radius of deformation of about 3–4 km, which explains the reduction of the signal at GW_6, 10 km away from the ice front (Figure 2c).

3.3. Implications

Away from the ice front, the ocean currents generally follow isobaths toward the ice shelf cavity (Assmann et al., 2019). At the ice front, the barotropic component of the current is redirected and follows the ice front (Wåhlin et al., 2020). The velocity at GW_{6F} is consequently reduced and only the baroclinic component, generally directed into the ice shelf cavity (Figures 3d–3h), continues across the ice front (Wåhlin et al., 2020). During the cold events, the ocean current accelerates and changes its direction and strength, especially at depth (Figure 3c). As expected in the absence of stratification, the current is more barotropic, and aligns roughly with the ice front throughout the whole water column (Figure 3c). The barotropic component accounts for up to 85% of the current speed at GW_{6F} during the events, compared to 59% ± 13% for the rest of W16 (for the calculation of the barotropic velocity, (see Wåhlin et al. (2020), method ii). This is also clear from Figures 3d–3h: For all depths, water colder than −1°C, that is, water from the surface layer, flows more parallel to the ice front compared to water warmer than 0°C, that is, water from the warm saline bottom layer, which flows more parallel to the bathymetry and enters the cavity. The events of deepened WW are characterized by reduced stratification, mainly barotropic currents, and strong blocking.

The simultaneous response of ocean temperature and velocities to strong easterly winds has implications on the heat transport into the ice shelf cavity. The strong reduction in heat content combined with the deflection of the current at the ice front reduces the heat transport into the cavity almost to zero during the events. The heat transport density into the ice shelf cavity averaged over W16 is about 120 MW m^{-1}. When the eight events are excluded, the mean heat transport density during the same time period increases to 160 MW m^{-1}; hence, the events reduce the heat transport over this period by 25%.

3.4. Interannual Variability

The heat content variability, the stratification, and the atmospheric forcing differ largely between 2016 and 2017 (Figure 2). The heat content in 2017 shows fewer and less pronounced drops compared to 2016, and only three events of deepened WW are identified (Figure 2c). In the beginning of the 2017 sea ice season (April–May), the heat content is persistently low due to wind-driven Ekman downwelling at the shelf break and suppressed CDW-flow onto the continental shelf (Assmann et al., 2019). At the end of the 2017 sea ice season (August–November), the heat content is higher compared to 2016, due to the lack of events of deepened WW. The period of locally high sea ice concentration is shorter in 2017 and has less polynyas compared to 2016 (Figure 2d). The different timing of sea ice growth is reflected in the salinity record of the uppermost sensor (288 m depth) that shows a gradual increase in salinity from August 2017, which is about three months later than in 2016 (Figure 2b).

The reduced number of events of deepened WW in 2017 compared to 2016 may be attributed to a different preconditioning of the water column and a reduced number of strong wind events during the sea ice period. The zonal wind in the winter of 2017 shows periods of strong easterly winds, but they are generally short and do not open a coastal polynya. The stronger wind events that coincide with a polynya opening, such as

the event in July 2017 and a longer period of reduced sea ice concentration in October 2017, only trigger a small response in the heat content (Figure 2d). An explanation of the weak response in 2017 to atmospheric forcing may be the combination of a shallower WW layer and strong stratification underneath (Figures 2a and 2b), which might reduce the wind effect on the thermocline depth. This suggests that the deepening of the WW occurs during years with a long sea ice season and frequent polynya openings that precondition the water column through a seasonal deepening of the WW.

The link between the events of deepened WW and atmospheric forcing suggests the use of the number of strong easterly wind events and/or coastal polynyas during each winter as a proxy for the maximum number of possible events. Although the events are wind-driven, the number of polynyas can be expected to be a good event indicator, as they incorporate both the strength and duration of easterly winds. An estimate of yearly variability in the number of events can thus be obtained from sea ice concentration and wind data extended over a longer time period (Figures S3b and S3c). Compared to a time period from 2003 to 2019, the winter of 2017 has the lowest number of winter polynyas and the second lowest number of strong easterly wind events (Figure S3a). Conditions similar to those observed in 2016 are more common, suggesting that this year, with frequent events of deepened WW, is more representative than 2017.

4. Conclusion

In this study, we investigated wind-driven fluctuations in heat supply to the base of the GIS in West Antarctica. We suggest that the observed intermittent deepening of the WW at the ice front is driven remotely by Ekman downwelling at the northern coast of Siple Island. Easterly winds cause Ekman convergence at the coast and trigger a coastal trapped wave that propagates along the coast and the ice front toward the mooring site. Due to the small internal Rossby radius of a few kilometers, this process can only be captured by moorings located close to the ice front (such as GW_{6F}) and by numerical models with a high enough resolution. Coastal trapped waves are a well-known phenomenon and have been observed along various coasts (e.g., Battisti & Hickey, 1984; Gelderloos et al., 2020; Inall et al., 2015; Robinson, 1964). Our results indicate that they are of particular importance around the coast of Antarctica, where the waves may block the inflow of warm bottom water into the ice shelf cavities as they travel along ice fronts. In regions with coastal Ekman upwelling, the opposite effect could be expected, leading to increased inflow of warm water. Due to the propagation of the signal, coastal Ekman downwelling, such as observed in the central Amundsen Sea (Kim et al., 2016), can influence ice shelves further west, even if the orientation of the ice front is not favorable for local coastal Ekman downwelling.

Ekman downwelling influences the inflow of CDW toward the Getz Ice Shelf on different time scales. Strong sustained easterly winds off the continental shelf deepen the thermocline at the shelf break and reduce the mean flow of CDW onto the continental shelf. The heat content at the ice front is thereby reduced with a time lag of about 5–6 days and on a weekly to monthly timescale (Assmann et al., 2019). In this study, we showed that strong events of along-shore winds cause an intermittent deepening of the thermocline and a westward propagation of the signal as a coastal trapped wave. The heat content at the ice front is reduced for about 5 days with a time lag of 3 days, and the along-ice shelf component of the current strengthens.

Variability in basal melting has been linked to changes in the thermocline depth at several ice shelves around Antarctica, for example, at the Wilkins Ice Shelf in the Bellinghausen Sea (Padman et al., 2012), at the Totten Ice Shelf in East Antarctica (Greene et al., 2017) and at the Pine Island Glacier in the eastern Amundsen Sea (Davis et al., 2018)—the latter also on short (weekly to monthly) timescales. Although the mooring observations at the western GIS front provide a good overview of the heat transport variability into the ice shelf cavity during 2016–2017, the circulation within the cavity and the amount of heat reaching the ice shelf base remain unknown. This highlights the need for concurrent observations of the shelf and sub-ice shelf circulation and basal melt rates.

Data Availability Statement

The GW_6 and GW_{6F} mooring data are available at the Norwegian Marine Data Center (https://nmdc.no) as UIB4 (Darelius et al., 2018) and at the SOOS database at NODC (Wåhlin et al., 2019a, 2019b), respectively.

References

Arndt, J. E., Schenke, H. W., Jakobsson, M., Nitsche, F. O., Buys, G., Goleby, B., et al. (2013). The international bathymetric chart of the Southern Ocean (IBCSO) version 1.0 - A new bathymetric compilation covering circum-Antarctic waters. *Geophysical Research Letters*, *40*(12), 3111–3117. https://doi.org/10.1002/grl.50413

Arneborg, L., Wåhlin, A. K., Björk, G., Liljebladh, B., & Orsi, A. H. (2012). Persistent inflow of warm water onto the central Amundsen shelf. *Nature Geoscience*, *5*(12), 876–880. https://doi.org/10.1038/ngeo1644

Årthun, M., Nicholls, K. W., & Boehme, L. (2013). Winter time water mass modification near an Antarctic ice front. *Journal of Physical Oceanography*, *43*(2), 359–365. https://doi.org/10.1175/JPO-D-12-0186.1

Assmann, K. M., Darelius, E., Wåhlin, A., Kim, T. W., & Lee, S. H. (2019). Warm circumpolar deep water at the western getz ice shelf front, Antarctica. *Geophysical Research Letters*, *46*(2), 870–878. https://doi.org/10.1029/2018GL081354

Battisti, D. S., & Hickey, B. M. (1984). Application of remote wind-forced coastal trapped wave theory to the Oregon and Washington coasts. *Journal of Physical Oceanography*, *14*(5), 887–903. https://doi.org/10.1175/1520-0485(1984)014⟨0887:AORWFC⟩2.0.CO;2

Darelius, E., Fer, I., Assmann, K., & Kim, T. W. (2018). *Physical oceanography from mooring UiB1 and UiB4 in the Amundsen sea*. https://doi.org/10.21335/NMDC-1721053841

Davis, P. E., Jenkins, A., Nicholls, K. W., Brennan, P. V., Abrahamsen, E. P., Heywood, K. J., et al. (2018). Variability in basal melting beneath pine island ice shelf on weekly to monthly timescales. *Journal of Geophysical Research: Oceans*, *123*(11), 8655–8669. https://doi.org/10.1029/2018JC014464

DeConto, R. M., & Pollard, D. (2016). Contribution of Antarctica to past and future sea-level rise. *Nature*, *531*(7596), 591–597. https://doi.org/10.1038/nature17145

Depoorter, M. A., Bamber, J. L., Griggs, J. A., Lenaerts, J. T., Ligtenberg, S. R., Van Den Broeke, M. R., & Moholdt, G. (2013). Calving fluxes and basal melt rates of Antarctic ice shelves. *Nature*, *502*(7469), 89–92. https://doi.org/10.1038/nature12567

De Rydt, J., Holland, P. R., Dutrieux, P., & Jenkins, A. (2014). Geometric and oceanographic controls on melting beneath pine island glacier. *Journal of Geophysical Research: Oceans*, *119*, 2420−2438. https://doi.org/10.1002/2013JC009513

Dotto, T. S., Naveira Garabato, A., Bacon, S., Tsamados, M., Holland, P. R., Hooley, J., et al. (2018). Variability of the ross gyre, southern ocean: Drivers and responses revealed by satellite altimetry. *Geophysical Research Letters*, *45*(12), 6195–6204. https://doi.org/10.1029/2018GL078607

Dotto, T. S., Naveira Garabato, A. C., Bacon, S., Holland, P. R., Kimura, S., Firing, Y. L., et al. (2019). Wind-driven processes controlling oceanic heat delivery to the Amundsen sea, Antarctica. *Journal of Physical Oceanography*, *49*(11), 2829–2849. https://doi.org/10.1175/jpo-d-19-0064.1

Dutrieux, P., De Rydt, J., Jenkins, A., Holand, P. R., Ha, H. K., Lee, S. H., et al. (2014). Strong sensitivity of pine island ice-shelf melting to climatic variability. *Science*, *174*, 174–179. https://doi.org/10.1126/science.1244341

Gelderloos, R., Haine, T. W. N., & Almansi, M. (2020). Coastal trapped waves and other subinertial variability along the southeast Greenland coast in a realistic numerical simulation. *Journal of Physical Oceanography*, *51*, 1–49. https://doi.org/10.1175/jpo-d-20-0239.1

Gill, A. E., & Clarke, A. J. (1974). Wind-induced upwelling, coastal currents and sea-level changes. *Deep-Sea Research and Oceanographic Abstracts*, *21*(5), 325–345. https://doi.org/10.1016/0011-7471(74)90038-2

Gille, S., McKee, D., & Martinson, D. (2016). Temporal changes in the Antarctic circumpolar current: Implications for the Antarctic continental shelves. *Oceanography*, *29*(4), 96–105. https://doi.org/10.5670/oceanog.2016.102

Greene, C. A., Blankenship, D. D., Gwyther, D. E., Silvano, A., & Wijk, E. V. (2017). Wind causes Totten ice shelf melt and acceleration. *Science Advances*, *3*, e1701681. https://doi.org/10.1126/sciadv.1701681

Gwyther, D. E., Galton-Fenzi, B. K., Hunter, J. R., & Roberts, J. L. (2014). Simulated melt rates for the Totten and Dalton ice shelves. *Ocean Science*, *10*(3), 267–279. https://doi.org/10.5194/os-10-267-2014

Haid, V., & Timmermann, R. (2013). Simulated heat flux and sea ice production at coastal polynyas in the southwestern Weddell Sea. *Journal of Geophysical Research: Oceans*, *118*(5), 2640–2652. https://doi.org/10.1002/jgrc.20133

Hersbach, H., Bell, B., Berrisford, P., Biavati, G., Horányi, A., Muñoz Sabater, J., et al. (2018). ERA5 hourly data on single levels from 1979 to present. *Copernicus climate change service (C3S) climate data store (CDS)*. https://doi.org/10.24381/cds.adbb2d47

Holland, P. R., Jenkins, A., & Holland, D. M. (2010). Ice and ocean processes in the Bellingshausen sea, Antarctica. *Journal of Geophysical Research*, *115*(5), 1–16. https://doi.org/10.1029/2008JC005219

Holte, J., & Talley, L. (2009). A new algorithm for finding mixed layer depths with applications to argo data and subantarctic mode water formation. *Journal of Atmospheric and Oceanic Technology*, *26*(9), 1920–1939. https://doi.org/10.1175/2009JTECHO543.1

Inall, M., Nilsen, F., Cottier, F., & Daae, R. (2015). Shelf/fjord exchange driven by coastal-trapped waves in the Arctic. *Journal of Geophysical Research: Oceans*, *120*, 8283–8303. https://doi.org/10.1002/2015JC011277

Jacobs, S. S., Giulivi, C. F., Dutrieux, P., Rignot, E., Nitsche, F., & Mouginot, J. (2013). Getz ice shelf melting response to changes in ocean forcing. *Journal of Geophysical Research: Oceans*, *118*(9), 4152–4168. https://doi.org/10.1002/jgrc.20298

Jacobs, S. S., Giulivi, C. F., & Mele, P. A. (2002). Freshening of the Ross sea during the late 20th century. *Science*, *297*(5580), 386–389. https://doi.org/10.1126/science.1069574

Jacobs, S. S., Jenkins, A., Hellmer, H., Giulivi, C., Nitsche, F., Huber, B., & Guerrero, R. (2012). The Amundsen sea and the Antarctic ice sheet. *Oceanography*, *25*(3), 154–163. https://doi.org/10.5670/oceanog.2012.90

Jenkins, A. (2016). A simple model of the ice shelf–ocean boundary layer and current. *Journal of Physical Oceanography*, *46*(6), 1785–1803. https://doi.org/10.1175/jpo-d-15-0194.1

Jenkins, A., Shoosmith, D., Dutrieux, P., Jacobs, S., Kim, T. W., Lee, S. H., et al. (2018). West Antarctic ice sheet retreat in the Amundsen sea driven by decadal oceanic variability. *Nature Geoscience*, *11*(10), 733–738. https://doi.org/10.1038/s41561-018-0207-4

Jourdain, N. C., Mathiot, P., Merino, N., Durand, G., Le Sommer, J., Spence, P., et al. (2017). Ocean circulation and sea-ice thinning induced by melting ice shelves in the Amundsen sea. *Journal of Geophysical Research: Oceans*, *122*(3), 2550–2573. https://doi.org/10.1002/2016JC012509

Khazendar, A., Schodlok, M. P., Fenty, I., Ligtenberg, S. R., Rignot, E., & Van Den Broeke, M. R. (2013). Observed thinning of Totten glacier is linked to coastal polynya variability. *Nature Communications*, *4*, 2857. https://doi.org/10.1038/ncomms3857

Kim, C. S., Kim, T. W., Cho, K. H., Ha, H. K., Lee, S. H., Kim, H. C., & Lee, J. H. (2016). Variability of the Antarctic coastal current in the Amundsen Sea. *Estuarine, Coastal and Shelf Science*, *181*, 123–133. https://doi.org/10.1016/j.ecss.2016.08.004

Kim, T. W., Ha, H. K., Wåhlin, A. K., Lee, S. H., Kim, C. S., Lee, J. H., & Cho, Y. K. (2017). Is Ekman pumping responsible for the seasonal variation of warm circumpolar deep water in the Amundsen Sea? *Continental Shelf Research*, *132*, 38–48. https://doi.org/10.1016/j.csr.2016.09.005

Kimura, N. (2004). Sea ice motion in response to surface wind and ocean current in the southern ocean. *Journal of the Meteorological Society of Japan*, *82*(4), 1223–1231. https://doi.org/10.2151/jmsj.2004.1223

Mazur, A. K., Wåhlin, A. K., & Kręzel, A. (2017). An object-based SAR image iceberg detection algorithm applied to the Amundsen sea. *Remote Sensing of Environment*, *189*, 67–83. https://doi.org/10.1016/j.rse.2016.11.013

McDougall, T., & Barker, P. (2011). Getting started with TEOS-10 and the Gibbs Seawater (GSW) Oceanographic Toolbox. *SCOR/IAPSO WG*, *127*, 1–28.

Nakayama, Y., Timmermann, R., Rodehacke, C. B., Schröder, M., & Hellmer, H. H. (2014). Modeling the spreading of glacial meltwater from the Amundsen and Bellingshausen Seas. *Geophysical Research Letters*, *41*(22), 7942–7949. https://doi.org/10.1002/2014GL061600

Ohshima, K. I., Nihashi, S., & Iwamoto, K. (2016). Global view of sea-ice production in polynyas and its linkage to dense/bottom water formation. *Geoscience Letters*, *3*(1), 13. https://doi.org/10.1186/s40562-016-0045-4

Padman, L., Costa, D. P., Dinniman, M. S., Fricker, H. A., Goebel, M. E., Huckstadt, L. A., et al. (2012). Oceanic controls on the mass balance of Wilkins Ice Shelf, Antarctica. *Journal of Geophysical Research: Oceans*, *117*(1), 1–17. https://doi.org/10.1029/2011JC007301

Paolo, F. S., Fricker, H. A., & Padman, L. (2015). Volume loss from Antarctic ice shelves is accelerating. *Science*, *348*(6232), 327–332. https://doi.org/10.1017/CBO9781107415324.004

Pritchard, H., Ligtenberg, S., Fricker, H., Vaughan, D., Van Den Broeke, M., & Padman, L. (2012). Antarctic ice-sheet loss driven by basal melting of ice shelves. *Nature*, *484*(7395), 502–505. https://doi.org/10.1038/nature10968

Raphael, M. N., Marshall, G. J., Turner, J., Fogt, R. L., Schneider, D., Dixon, D. A., et al. (2016). The Amundsen sea low: Variability, change, and impact on Antarctic climate. *Bulletin of the American Meteorological Society*, *97*(1), 111–121. https://doi.org/10.1175/BAMS-D-14-00018.1

Reese, R., Gudmundsson, G. H., Levermann, A., & Winkelmann, R. (2018). The far reach of ice-shelf thinning in Antarctica. *Nature Climate Change*, *8*(1), 53–57. https://doi.org/10.1038/s41558-017-0020-x

Rignot, E., Jacobs, S., Mouginot, J., & Scheuchl, B. (2013). Ice-shelf melting around Antarctica. *Science*, *341*(6143), 266–270. https://doi.org/10.1126/science.1235798

Rignot, E., Mouginot, J., Scheuchl, B., Van Den Broeke, M., Van Wessem, M. J., & Morlighem, M. (2019). Four decades of Antarctic ice sheet mass balance from 1979–2017. *Proceedings of the National Academy of Sciences of the United States of America*, *116*(4), 1095–1103. https://doi.org/10.1073/pnas.1812883116

Robinson, A. R. (1964). Continental shelf waves and the response of sea level to weather systems. *Journal of Geophysical Research*, *69*(2), 367–368. https://doi.org/10.1029/JZ069i002p00367

Schaffer, J., Timmermann, R., Erik Arndt, J., Savstrup Kristensen, S., Mayer, C., Morlighem, M., & Steinhage, D. (2016). A global, high-resolution data set of ice sheet topography, cavity geometry, and ocean bathymetry. *Earth System Science Data*, *8*(2), 543–557. https://doi.org/10.5194/essd-8-543-2016

Silvano, A., Rintoul, S. R., Peña-Molino, B., Hobbs, W. R., van Wijk, E., Aoki, S., et al. (2018). Freshening by glacial meltwater enhances melting of ice shelves and reduces formation of Antarctic bottom water. *Science Advances*, *4*(4), eaap9467. https://doi.org/10.1126/sciadv.aap9467

Spence, P., Griffies, S. M., England, M. H., Hogg, A. M. C., Saenko, O. A., & Jourdain, N. C. (2014). Rapid subsurface warming and circulation changes of Antarctic coastal waters by poleward shifting winds. *Geophysical Research Letters*, *41*(13), 4601−4610. https://doi.org/10.1002/2014GL060613.Received

Spreen, G., Kaleschke, L., & Heygster, G. (2008). Sea ice remote sensing using AMSR-E 89-GHz channels. *Journal of Geophysical Research*, *113*(2), 1–14. https://doi.org/10.1029/2005JC003384

Steig, E. J., Ding, Q., Battisti, D. S., & Jenkins, A. (2012). Tropical forcing of circumpolar deep water inflow and outlet glacier thinning in the Amundsen sea embayment, west Antarctica. *Annals of Glaciology*, *53*(60), 19–28. https://doi.org/10.3189/2012AoG60A110

St-Laurent, P., Klinck, J., & Dinniman, M. (2015). Impact of local winter cooling on the melt of Pine island glacier, Antarctica. *Journal of Geophysical Research: Oceans*, *120*(10), 6718−6732. https://doi.org/10.1002/2015JC010709

Sverdrup, H. (1953). The currents off the coast of Queen Maud Land. *Norsk Geografisk Tidsskrift-Norwegian Journal of Geography*, *14*(1–4), 239−249. https://doi.org/10.1080/00291955308542731

Thoma, M., Jenkins, A., Holland, D., & Jacobs, S. (2008). Modeling circumpolar deep water intrusions on the Amundsen sea continental shelf, Antarctica. *Geophysical Research Letters*, *35*(18), 2–7. https://doi.org/10.1029/2008GL034939

Tschudi, M. A., Meier, W. N., & Scott Stewart, J. (2020). An enhancement to sea ice motion and age products at the national snow and ice data center (NSIDC). *The Cryosphere*, *14*(5), 1519–1536. https://doi.org/10.5194/tc-14-1519-2020

Tschudi, M. A., Meier, W. N., Stewart, J. S., Fowler, C., & Maslanik, J. (2019). Polar pathfinder daily 25 km EASE-grid sea ice motion vectors. *National snow and ice data center distributed active archive center*, Boulder, Colorado: NASA. https://doi.org/10.5067/INAWUWO7QH7B

Wåhlin, A. K., Kalén, O., Arneborg, L., Björk, G., Carvajal, G. K., Ha, H. K., et al. (2013). Variability of warm deep water inflow in a submarine trough on the Amundsen sea shelf. *Journal of Physical Oceanography*, *43*(10), 2054–2070. https://doi.org/10.1175/JPO-D-12-0157.1

Wåhlin, A. K., Rolandsson, J., & Assmann, K. M. (2019a). *Horizontal components of current velocity collected by ADCP from a mooring deployed and recovered by research vessel ice breaker Araon in the Amundsen Sea from 2016-01-28 to 2018-01-18*. NOAA National Centers for Environmental Information, Dataset(Dataset), Dataset. https://doi.org/10.25921/n07g-f935

Wåhlin, A. K., Rolandsson, J., & Assmann, K. M. (2019b). *Water temperature, salinity, oxygen, and other oceanographic data collected by CTD from a mooring deployed and recovered by the research vessel ice breaker Araon in the Amundsen sea from 2016-01-28 to 2018-01-18*. NOAA National Centers for Environmental Information(Dataset), Dataset. https://doi.org/10.25921/6pwp-1791

Wåhlin, A. K., Steiger, N., Darelius, E., Assmann, K. M., Glessmer, M. S., Ha, H. K., et al. (2020). Ice front blocking of ocean heat transport to an Antarctic ice shelf. *Nature*, *578*, 568–571. https://doi.org/10.1038/s41586-020-2014-5

Wåhlin, A. K., Yuan, X., Björk, G., & Nohr, C. (2010). Inflow of warm circumpolar deep water in the central Amundsen shelf. *Journal of Physical Oceanography*, *40*(6), 1427–1434. https://doi.org/10.1175/2010JPO4431.1

Walker, D. P., Brandon, M. A., Jenkins, A., Allen, J. T., Dowdeswell, J. A., & Evans, J. (2007). Oceanic heat transport onto the Amundsen sea shelf through a submarine glacial trough. *Geophysical Research Letters*, *34*(2), 2–5. https://doi.org/10.1029/2006GL028154

Webber, B. G., Heywood, K. J., Stevens, D. P., & Assmann, K. M. (2019). The impact of overturning and horizontal circulation in Pine island trough on ice shelf melt in the eastern Amundsen sea. *Journal of Physical Oceanography*, *49*(1), 63–83. https://doi.org/10.1175/JPO-D-17-0213.1

Webber, B. G., Heywood, K. J., Stevens, D. P., Dutrieux, P., Abrahamsen, E. P., Jenkins, A., et al. (2017). Mechanisms driving variability in the ocean forcing of Pine island glacier. *Nature Communications*, *8*, 1–8. https://doi.org/10.1038/ncomms14507